



Cite this: DOI: 10.1039/d2ee00571a

Imidazole additives in 2D halide perovskites: impacts of $-CN$ versus $-CH_3$ substituents reveal the mediation of crystal growth by phase buffering[†]

Shuang Yu,^a Jie Meng,^b Qinying Pan,^c Qian Zhao,^b Tõnu Pullerits,^c Yingguo Yang,^b* Kaibo Zheng^b* and Ziqi Liang^b*^a

The unique sandwich structure and favorable crystallization kinetics have endowed two-dimensional (2D) halide perovskites with excellent ambient stability and facile film formation compared to those of their three-dimensional counterparts. However, the heterogeneous crystallization of multiple n -value phases during solution-casting of 2D perovskite thin films results in random and disordered crystalline alignment in conjunction with numerous lattice defects, all of which ultimately impair the device performance. Herein we demonstrate that highly ordered lattice arrangements in 2D lead halide perovskites, exemplified as a paradigm phenylethylamine (PEA) spacer, can be achieved using the 4,5-dicyanoimidazole (DCI) additive without any post-treatment. Electrostatic potential distribution mapping and X-ray photoelectron spectroscopy collectively confirm the Lewis acid–base interaction between $-CN^-$ units in DCI and Pb^{2+} , which is conducive to homogeneous nucleation during perovskite crystallization. A sequence of *in situ* grazing-incident wide-angle X-ray scattering and high-resolution transmission electron microscopy characterization unravel the epitaxial growth of multi-phases that gradually buffer the internal lattice strain and consequently regulate the lattice orientation, which markedly leads to a reduction of trap density and a prolongation of carrier lifetime. The resulting planar solar cells based on 2D $PEA_2MA_2Pb_3I_{13}$ ($n = 4$) deliver an outstanding efficiency of $\sim 17.0\%$ along with excellent operational stability.

Received 19th February 2022,
Accepted 7th June 2022

DOI: 10.1039/d2ee00571a

rsc.li/ees

Broader context

The unique sandwich structure endows 2D halide perovskites with outstanding moisture resistance compared to that of their 3D counterparts. However, the performance of 2D perovskite solar cells is still largely behind that of 3D analogues, which is mainly attributed to the mixed-dimensionality phases in thin films and inefficient charge transport among them. Much effort has been devoted to tackle these issues by improving the lattice arrangement or weakening the quantum confinement of layered halide perovskites. However, these strategies would inevitably introduce defects that hinder interlayer charge transportation and hence become the bottleneck for the device performance. In this contribution, we discover that the lattice arrangement of 2D halide perovskites can be optimized by such a phase-buffering process that involves mild epitaxial growth among different n -valued phases. This phase buffering is enabled by a newly-proposed 4,5-dicyanoimidazole (DCI) additive for favorably modulating the crystallization process. The consequent 2D $PEA_2MA_2Pb_3I_{10}$ ($n = 4$, PEA-4) based solar cells achieve a best power conversion efficiency approaching $\sim 17\%$ without any post-treatment, which represents a $\sim 50\%$ improvement over that of neat PEA-4. This work provides an alternate avenue to highly efficient and stable 2D perovskite solar cells.

^a Department of Materials Science, Fudan University, Shanghai 200433, China.
E-mail: zqliang@fudan.edu.cn

^b Department of Chemistry, Technical University of Denmark, DK-2800 Kongens Lyngby, Denmark. E-mail: kzhang@kemi.dtu.dk

^c Department of Chemical Physics and NanoLund, Lund University, Box 124, 22100 Lund, Sweden

^d Shanghai Synchrotron Radiation Facility (SSRF), Shanghai Advanced Research Institute & Chinese Academy of Sciences, Shanghai 201204, China.

E-mail: yangyingguo@sinap.ac.cn

† Electronic supplementary information (ESI) available: Supplementary videos available. See DOI: <https://doi.org/10.1039/d2ee00571a>

Introduction

Two-dimensional (2D) halide perovskites have received increasing attention thanks to their ambient stability superior to that of the three-dimensional (3D) analogs; however, the record power conversion efficiency (PCE) of 2D perovskites ($\sim 18\%^{1-3}$) is still much lower than that of their 3D counterpart ($25.7\%^4$). The underlying bottlenecks are believed to originate primarily from two issues: (1) the long-chain spacer molecules between inorganic octahedra

hinder exciton splitting and interlayer charge transport;⁵ (2) the randomly-oriented 2D lattices impede charge transport along the working direction in devices.⁶ The first can be tackled by a rational design of spacer molecules to modulate the electronic structures and crystallinity of 2D perovskites and hence ensure efficient interphase carrier transfer.^{7–15} As far as the second issue is concerned, by contrast, regulating the lattice arrangement in 2D perovskites remains to be a grand challenge.

A paradigm type of 2D halide perovskite is the Ruddlesden-Popper perovskite (RPP) that presents a component formula of $L'_2A_{n-1}B_nX_{3n+1}$ where L' represents the organic cation, A and B refer to monovalent and divalent cations, respectively, X is a halide anion, and n denotes the number of inorganic octahedral $[BX_6]^{4-}$ layers.¹⁶ Additional organic spacers L' ineluctably retard the 2D perovskite crystal growth relative to 3D counterparts, resulting in small-sized grains and numerous grain boundaries, which make it difficult to obtain pinhole- and defect-free thin films.¹⁷ In particular, 2D perovskite crystallization involves various degrees of $[BX_6]^{4-}$ octahedral aggregation along with random orientation, which lead to disordered phase arrangements.¹⁸ The resulting multiple- n valued low-dimensional phases with varying $[BX_6]^{4-}$ distortion in terms of the B-X-B angles¹⁹ give rise to the accumulation of lattice strain on interphase boundaries and therefore largely disturb the long-range ordering of perovskite lattices.²⁰ As such, the disordered multiple phases and undesirable lattice strain during thin-film formation would inevitably induce boundary traps as nonradiative recombination centers, constraining exciton splitting and carrier transport.²¹ A notable strategy of lattice regulation in 2D perovskites has been focused on either controlling the super-saturation kinetics by hot-casting²² and/or post-thermal-annealing,²³ or adding an intermediate state *via* the DMSO co-solvent to slow down the crystallization process.²⁴ However, the origin of the lattice randomization or strain accumulation in 2D perovskites largely remains elusive. In this work, we demonstrate that the lattice arrangement of 2D halide perovskites can be effectively modulated by phase buffering, which involves a mild epitaxial growth among low- n phases *via* crystallization modulation enabled by a newly proposed 4,5-dicyanoimidazole (DCI) additive.

Arguably, the crystallization process of 2D halide perovskites entails a longer time due to the incorporation of additional organic spacer cations between the inorganic octahedra layers when compared to the 3D analogues. According to the Lewis acid-base theory, Pb^{2+} as a soft Lewis acid^{25,26} coordinates with a Lewis base to form an intermediate phase and thus prolongs the perovskite crystallization process, whereas the chloride anion (Cl^-) has proved to be effective as a Lewis base. Chlorinated additives have been introduced to modulate the crystallization of 2D perovskites.^{27,28} For instance, Chen *et al.* found that the methylammonium chloride (MACl) additive facilitated the growth of near-single-crystal nanorod-like crystals with preferentially perpendicular orientation in 2D $(ThMA)_2(MA)_2Pb_3I_{10}$ RPPs *via* forming an intermediate phase.²⁹ However, the crystallization process of 2D perovskites with the aid of an additive usually requires complex and uncontrollable pre/post-treatments, such as thermal-annealing and/or hot-casting, to

remove the excess of MACl additive. Our previous studies, on the other hand, unveiled the effect of a volatile NH_4Cl additive at room temperature on improving the phase orientation and crystallization in 2D $PEA_2MA_3Pb_4I_{13}$ ($n = 4$) RPPs.²⁴ The additive exploited in this study featuring a much strongly polarized soft Lewis base $-CN^-$ can more easily donate electrons to Pb^{2+} compared to the hard Lewis base Cl^- according to soft-hard acid-base theory. It is revealed that the DCI additive promotes the epitaxial growth of low- n phases along the growth direction to release internal lattice strain, and finally regulates lattice orientation as well as reduces interfacial defects. As a proof-of-concept, the p-i-n architecture planar solar cells based on DCI-treated 2D $PEA_2MA_3Pb_4I_{13}$ ($n = 4$) RPPs without any post-treatment exhibit the best PCE of 17.0% under AM 1.5G light illumination, which is mainly attributed to the diminished trap states and the well-ordered lattice arrangement.

Results and discussion

The neat 2D $PEA_2MA_3Pb_4I_{13}$ ($n = 4$) RPP thin-films were fabricated by one-step spin-coating from mixed DMF:DMSO (100:3 vol%) solvents at room temperature without any post-treatment. Likewise, additive-treated 2D RPP films were made by adding the DMI and DCI molecules to the 2D RPP precursor. For brevity, $PEA_2MA_3Pb_4I_{13}$ ($n = 4$), DMI- and DCI-treated $PEA_2MA_3Pb_4I_{13}$ are denoted as PEA-4, PEA-4|DMI, and PEA-4|DCI, respectively.

Fig. 1a shows the molecular models of imidazole-based DMI and DCI additives. With the aid of cyanogen ($-CN$), the dipole moment of DCI (~7.2 Debye) is twice larger than that of DMI (~3.6 Debye), indicative of its stronger polarity. To elucidate the active role of $-CN$ among additive molecules, we utilized electrostatic potential (ESP) maps to analyze the electronic structures, as shown in Fig. 1b. The corresponding electronegativity distributions of each atom in both DMI and DCI additives are summarized in Fig. S1 (ESI†). The two $-CN$ substituent groups in DCI act as strong negative charge centers (highlighted as red and yellow regions) while methyl ($-CH_3$) units in DMI show an inhomogeneous electron density distribution, suggesting that the $-CN^-$ units in DCI could coordinate with Pb^{2+} in perovskite octahedral cages $[PbI_6]^{4-}$ *via* forming a Lewis acid-base pair. Note that the $-CN$ near the single-bond linked nitrogen atom in $-NH-$ linkage exhibits a stronger negative-charge concentration of -0.890 than the other near the double-bond linked nitrogen atom ($=N-$) (-0.855). This is further confirmed by density functional theory (DFT) calculations on the Lewis acid-base coordination between DCI and PbI_2 , which mainly occurs on both $-NH-$ and that near $-CN$, as shown in Fig. S2 (ESI†). As for the DMI additive, in contrast, the active site that interreacts with Pb^{2+} is located at the imidazole ring.

Such different coordination is experimentally supported by the X-ray photoelectron spectroscopy (XPS) spectra. As shown in Fig. S3 (ESI†), both DMI and DCI treated PbI_2 exhibit a shift to lower binding energy (E_B) relative to neat PbI_2 suggesting that both additives could react with PbI_2 . Upon an inclusion of an additive into PEA-4, as shown in Fig. S4 (ESI†), DCI lowers the

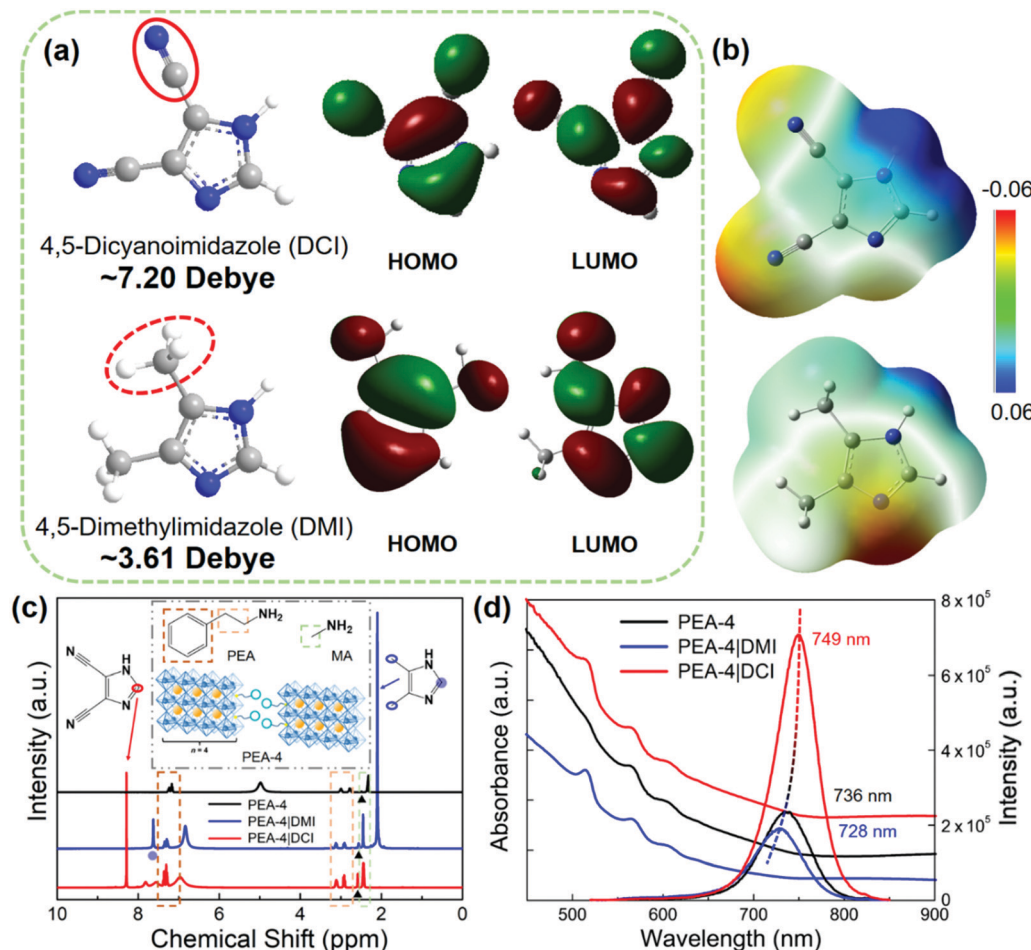


Fig. 1 Imidazole-based additives treated 2D $\text{PEA}_2\text{MA}_3\text{Pb}_4\text{I}_{13}$ perovskites. (a) Dipole moments as well as LUMO and HOMO energy levels, and (b) ESP distribution maps of imidazole-based additives. Note that blue, gray and white balls represent nitrogen, carbon, and hydrogen atoms, respectively. (c) ¹H-NMR spectra of both neat and treated 2D PEA-4 perovskite structures schematically shown in the insets for identifying the PEA/MA cation and the DMI/DCI additive. (d) Steady-state optical absorption and PL spectra in thin films.

E_{BS} of Pb 4f_{7/2} and 4f_{5/2} peaks in PEA-4|DCI down to 138.0 eV and 142.8 eV, respectively, implying that DCI indeed coordinates with under-coordinated Pb²⁺; in contrast, such an effect is absent in PEA-4|DMI, which is interpreted as follows: it is noteworthy that the =N- and -NH- units in the imidazole ring also present negative charge concentration in both additive molecules, in which the negative intensities in DMI (-0.32 and -0.41, corresponding to =N- and -NH- moieties, respectively) are higher than those in DCI (-0.26 and -0.38), as shown in Fig. S1 (ESI[†]). The coordination of these two units with the [PbI₆]⁴⁻ octahedra is however difficult by considering that the steric hindrance near the active nitrogenous group inhibits the penetration of ammonium into the inorganic sheets.³⁰

Furthermore, ¹H-nuclear magnetic resonance (NMR) spectra were obtained to compare the effects of DMI and DCI on the molecular structure of PEA-4 perovskites when dissolved in the DMSO-d₆ solvent, as shown in Fig. 1c. To amplify the effect of additives, the molar ratios of DMI and DCI in the precursor solution are increased. The pristine PEA-4 sample displays ¹H signals of DMSO-d₆ (~2.49 ppm), PEA (2.77, 2.99, 7.15–7.25 ppm) and MA (2.33 ppm), respectively, which coincide with the

theoretical values as predicted using ChemDraw software as shown in Fig. S5 (ESI[†]). Upon the addition of DMI and DCI, all peaks show chemical shifts to a lower-field, suggesting that the electron density is decreased. Note that the peak shifts of PEA and MA (~0.12 ppm) are larger than that of DMSO-d₆ (~0.08 ppm), which excludes the possibility of a monolithic shift.

Fig. 1d presents the optical absorption and photoluminescence (PL) spectra of all three samples in thin films. They all show pronounced excitonic absorption peaks, referred to as the excitonic states of the 2D perovskite phases, in which the films with DMI and DCI treatments exhibit higher absorbance at ~510 nm (*i.e.*, $n = 1$). Note that PEA-4|DCI exhibits the strongest visible-light (400–800 nm) absorption under the same film thickness of ~328 nm as measured using a step profiler, as shown in Fig. S6 (ESI[†]). It is also seen that a dominant emission band of pristine PEA-4 is located at 736 nm. The emission of PEA-4|DCI shows a noticeable red-shift to 749 nm with the strongest PL intensity among three samples, indicating the generation of more 3D-like phases with less nonradiative recombination relative to neat PEA-4, while PEA-4|DMI displays the weakest PL peak with a blue-shift to 728 nm.

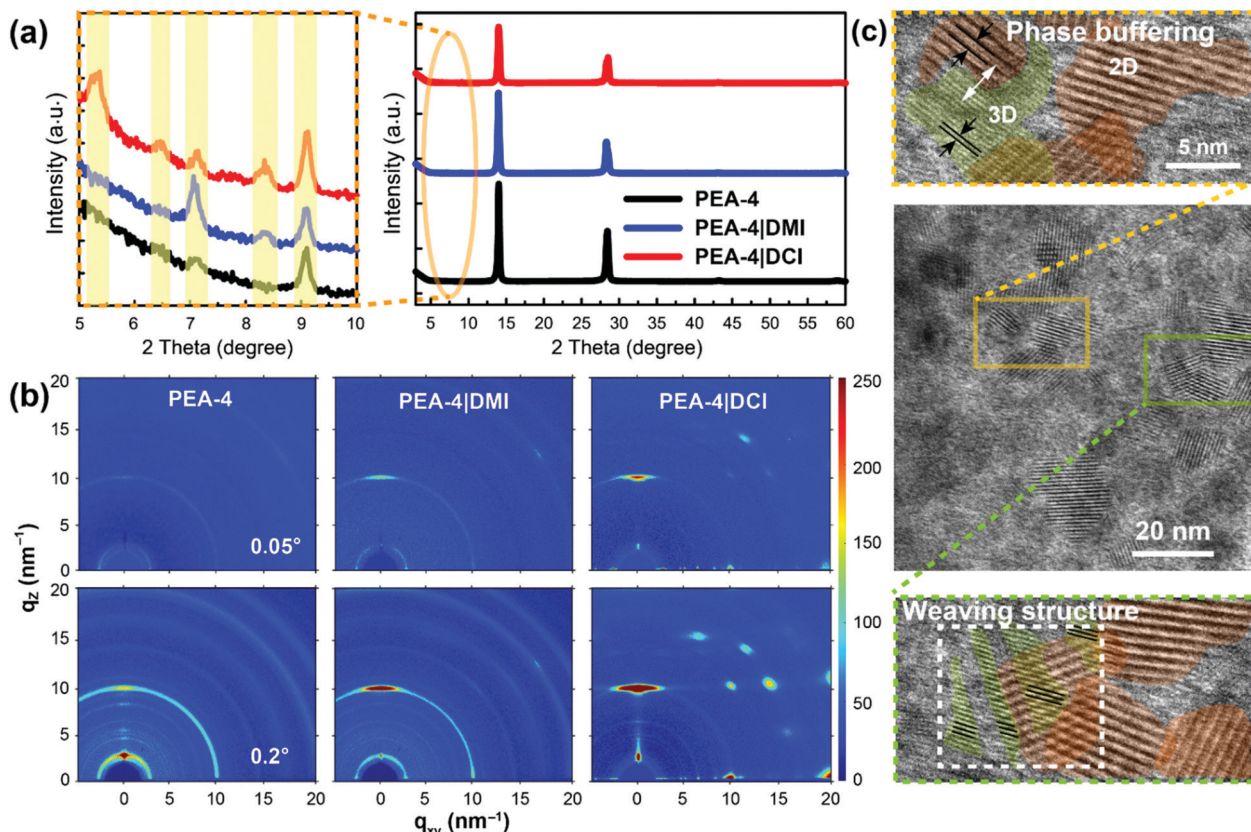


Fig. 2 Crystal structures and thin-film morphologies. (a) XRD patterns, (b) GIWAXS diffraction patterns at incident angles of 0.05° (surface) and 0.2° (bulk), respectively. (c) HR-TEM images of DCI-treated PEA-4 featuring the phase transition process and internal weaving structure.

Next, we investigated the crystallinity, orientation and morphological features of the three samples. The X-ray diffraction (XRD) patterns are shown in Fig. 2a, showing two characteristic perovskite peaks at ~ 14 and 28° for all samples. The use of an additive, either DMI or DCI, does not change the inorganic octahedral $[\text{PbI}_6]^{4-}$ crystal structure, as evidenced by the negligible shift of characteristic peaks, while the crystallinity is slightly decreased with a broadening of full width at half maxima (FWHM), as summarized in Table S1 (ESI†). In order to exclude the possible effects of MA cations on inorganic $[\text{PbI}_6]^{4-}$ cages, the XRD profiles of pure 2D PEAPbI₄ perovskites (*i.e.*, $n = 1$, denoted as PEA-1) are obtained as shown in Fig. S7 (ESI†). It is unveiled that the characteristic 2D phase peak at $\sim 5^\circ$ and its FWHM both remain unchanged after DMA and DCI treatments. In addition, two diffraction peaks below 10° (that is, 7.14° and 9.10°) appear in neat PEA-4 as well as DMI- and DCI-treated PEA-4 samples, as shown in the enlarged XRD patterns marked in Fig. 1a, suggesting the identical structural characteristics of 2D perovskites. After DMI treatment, the intensity of the peak at 7.14° is strengthened and an additional new peak located at 8.34° appears. Likewise, these two peaks are found in the PEA-4|DCI sample, along with two other extra peaks at 5.28° and 6.46° . In short, the number of low-dimensional perovskite phases is gradually increased from PEA-4 to DMI-treated and then DCI-treated PEA-4 films. Field-emission scanning electron microscopy (FE-SEM) imaging was further employed to explain how such a

trend of low-dimensional perovskite crystallization affects the film morphology. As shown in Fig. S8 (ESI†), PEA-4 presents rod-like crystal clusters, which further grow larger after DMI and DCI treatments with the largest and densest clusters shown in PEA-4|DCI. Moreover, as shown in Fig. 2b, pristine PEA-4 shows a distinct spot-like diffraction ring at $q \sim 10 \text{ nm}^{-1}$ (*i.e.*, the perovskite phase) with an incident angle of 0.2° ; in contrast, such a ring is negligible at 0.05° . The incident angles of 0.05° and 0.2° refer to the penetration depths of ~ 5 and $\sim 100 \text{ nm}$, respectively.³¹ The incident angle of 0.05° detects only surface orientation information at a depth of $\sim 5 \text{ nm}$, while 0.2° can detect a superposition of all information from 2 to $\sim 100 \text{ nm}$. Thus, the signal is sharper at 0.2° than at 0.05° . Upon the addition of DMI, the diffraction ring is intensified, in particular at $q_z \sim 10 \text{ nm}^{-1}$ whose signal is quite noticeable even with a low incident angle of 0.05° . In PEA-4|DCI, these effects are further reinforced with sharp and discrete spots appearing at $q_{xy} \sim 10$ and 20 nm^{-1} , suggesting a high degree of vertically-orientated perovskite phases. Moreover, the spot-like signal of the low- n phase at $q_z \sim 3 \text{ nm}^{-1}$ in PEA-4|DCI suggests a highly-ordered low- n phase alignment compared to random diffraction rings found in both PEA-4 and PEA-4|DMI samples. Such aligned low- n phases as well as vertically orientated perovskite phases would greatly benefit charge carrier transport along the work direction in solar cells.

In order to offer an in-depth characterization of the above crystal structure on the nanometer scale, high-resolution

transmission electron microscopy (HR-TEM) images are obtained as shown in Fig. 2c and the corresponding interplanar spacings of enlarged regions are summarized in Fig. S9 (ESI†). All three samples exhibit 2D perovskite phases with distinct lattice fringes as shown in Fig. S10 (ESI†), in which the region of 2D phases in PEA-4|DCI is the largest among the three samples. As shown in Fig. 2c, PEA-4|DCI presents a phase transition between 2D and 3D phases with the same orientation of lattice fringes such that it could act as phase buffering to release the undesirable interphase strain effectively. Surprisingly, we found the weaving structures in PEA-4|DCI as highlighted in Fig. 2c, that is, the 3D phases with the same lattice fringe direction are evenly interspersed within the 2D phases. Such a phenomenon could be circumstantial evidence for phase transition, while the Moire fringe arising from stacked phases with different directed orientations is another possibility that cannot be eliminated.

Time-resolved *in situ* GIWAXS analysis was then implemented to unravel the intrinsic crystallization kinetics of such phase buffering phenomenon during thin-film spin-coating, which will offer a deep insight into the evolution from precursor to crystal nucleus and finally crystallized films, as presented in Fig. 3. It should be pointed out that owing to the slightly deviated environment during *in situ* GIWAXS measurement, including ambient temperature, humidity, atmosphere, etc., the entire crystallization shows to be slightly longer than that under the conditions of device fabrication, that is, within a N₂-filled glovebox at a low concentration of oxygen and water. The crystallization process can be divided into three stages of precursors, nucleation and crystal growth as shown in Fig. 3a, according to the azimuthally integrated profiles. (1) An initial stage of precursor-sol-gel is observed as a broad low-angle scattering signal after a drop of precursor solution on the substrate at ~2 s. PEA-4|DMI requires more time (28 s) in the precursor stage compared to the other two samples (22 s), implying that a higher energy barrier caused by density fluctuation needs to be overcome in the initial formation of the crystal nucleus. To determine the starting point of nucleation, 2D GIWAXS profiles for each 0.5 s during spin-coating are analyzed in the supplementary videos (namely, PEA-4, DMI-treated PEA-4, and DCI-treated PEA-4, ESI†) and the corresponding key nodes are shown in Fig. 3b. (2) For the nucleation process, in PEA-4|DCI, the low-*n* phase at $q_z \sim 6 \text{ nm}^{-1}$, assigned to $n = 2$,³² first begins to nucleate followed by the perovskite phase ($q_z \sim 10 \text{ nm}^{-1}$) after 2 s, analogous to the pristine PEA-4 sample, while perovskite and multiple-*n* valued phases ($q_z \sim 5, 6, 7 \text{ nm}^{-1}$) nucleate simultaneously in the PEA-4|DMI film. (3) During the crystal growth process, the control PEA-4 sample shows an intermediate low-*n* phase at $q_z \sim 3 \text{ nm}^{-1}$ before the crystallization is completed, which disappears in the final thin film. With the addition of DMI, the crystal growth process is so fast that no significant variation is observed during crystallization, as shown in Fig. 3c. It is also found in the integral curves that only PEA-4|DMI exhibits an excess of the PbI₂ phase at $q_z \sim 8\text{--}9 \text{ nm}^{-1}$ in the evolution from crystal nucleus to thin film.³¹

Interestingly, for PEA-4|DCI, there is a transformation of low-*n* phases from $q_z \sim 5, 6, 7 \text{ nm}^{-1}$ to 3 nm^{-1} during the

crystal growth process, which is in accordance with the phase buffering phenomenon uncovered in the HR-TEM images. In particular, Fig. 3d shows the integral intensity profiles of low-*n* phases, revealing that such a buffering process occurs from the starting point of crystal growth at 27 s to the final crystallized thin film (46 s). The evolution of 2D GIWAXS patterns during the phase buffering process is summarized in Fig. S11 (ESI†). In the crystallized thin film, as shown in Fig. 3e, it is worth noting that the DCI-treated sample exhibits the strongest crystallinity of perovskite phases among all samples. In short, the detailed phase buffering process during the crystallization process is proposed in Scheme S1 (ESI†). Notably, the DCI/DMI additive could interact with PbI₂ to form such intermediate Lewis acid–base pairs that effectively modulate the crystallization process. Since the active site of the imidazole ring in DMI sterically hinders the incorporation into 2D perovskite lattices, PEA-4|DMI tends to form the accumulated strain, resulting in multiphase competing nucleation and the subsequent ultra-fast crystallization growth process. In contrast, the active site of DCI is situated in the –CN group, which has a smaller steric hindrance than the imidazole ring, thereby leading to the sequential process of nucleation and phase buffering during crystal growth.

The phase buffering effect on the charge carrier dynamics of 2D RPPs is further explored by binding energy (E_B) measurement and time-resolved spectroscopies (please refer to the details in the Experimental section). The E_B of PEA-4|DCI is determined by a linear fitting of the dominant PL peak intensity as a function of temperature to be 111.4 meV, which is substantially smaller than those of neat PEA-4 and PEA-4|DMI samples (*i.e.*, 202.5 and 348.5 meV, respectively) (Fig. 4a). The largest E_B value caused by the DMI treatment can be ascribed to large steric hindrance between the active ==N– site in the DMI imidazole ring and the central Pb²⁺ in the inorganic octahedral [Pb₆]^{4−} cage.³³ On the basis of determined E_B values, we can further estimate the equilibrium ratio between free charge carriers and photogenerated excitons according to the Saha–Langmuir theory.³⁴ Here the fraction of free charges over the total density of excitation (x) can be expressed as follows:

$$\frac{x^2}{1-x} = \frac{1}{n} \left(\frac{2\pi m k_B T}{h^2} \right)^{1.5} e^{-\frac{E_B}{k_B T}} \quad (1)$$

where x is the ratio of the free charges over the total density of excitation, n is the sum of free charge carriers (n_{FC}) and excitons (n_{exc}) giving the excitation density, m is the reduced mass of the exciton (~0.15 m_e), E_B is exciton binding energy, h is Planck's constant, and T is the temperature. Notably, as shown in Fig. 4b, PEA-4|DCI exhibits the largest free charge ratio among total photo-excited carriers, thereby promoting carrier transport. Moreover, we exploited time-resolved spectroscopies to unravel the origins of charge transportation and energy transfer. Fig. 4c shows time-resolved photoluminescence (TRPL) decays, in which the average lifetime (τ) can be divided, *via* bi-exponential fitting (eqn (2)), into two components—fast τ_1 and slow τ_2 ; the former refers to defect-assisted non-radiative recombination while the latter relates to radiative recombination. It is seen that PEA-4|DCI

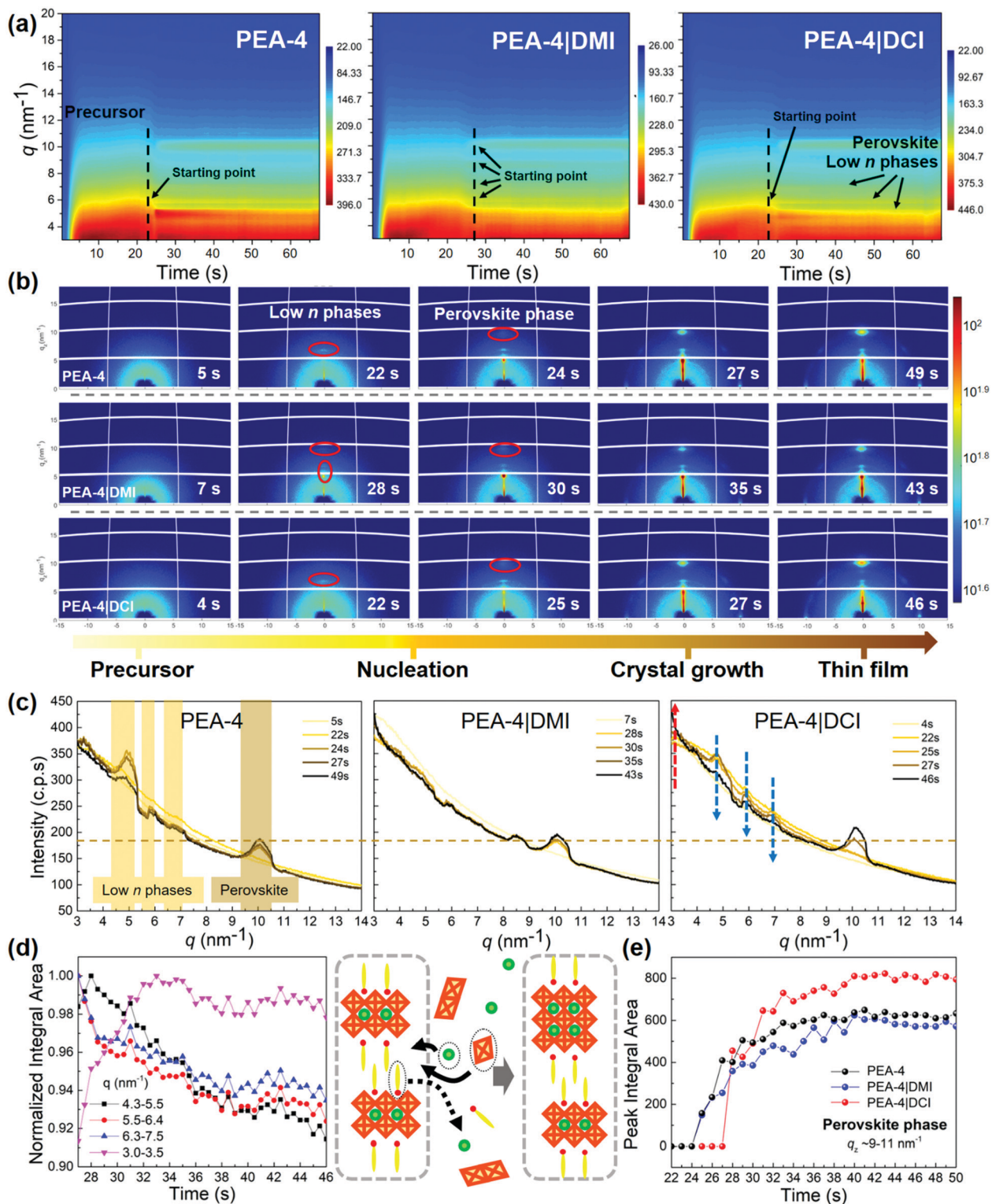


Fig. 3 Crystallization kinetics probed by *in situ* GIWAXS measurements. (a) Time evolution of operando synchrotron radiation-based GIWAXS data plotted as azimuthally integrated line profiles, (b) the corresponding 2D GIWAXS patterns, and (c) integrated curves over all azimuthal angles of the crystallization process over time. The colour line from light to dark refers to the precursor, the nucleation process (low- n phases and perovskite phase), the crystal growth, and the final crystallized thin film. (d) Phase buffering: low- n phases' intensity evolution during the crystallization process in DCI-treated PEA-4 samples and the corresponding scheme. (e) Perovskite peak's integral area of neat PEA-4, DMI- and DCI-treated PEA-4 from $q_z \sim 9\text{--}11 \text{ nm}^{-1}$.

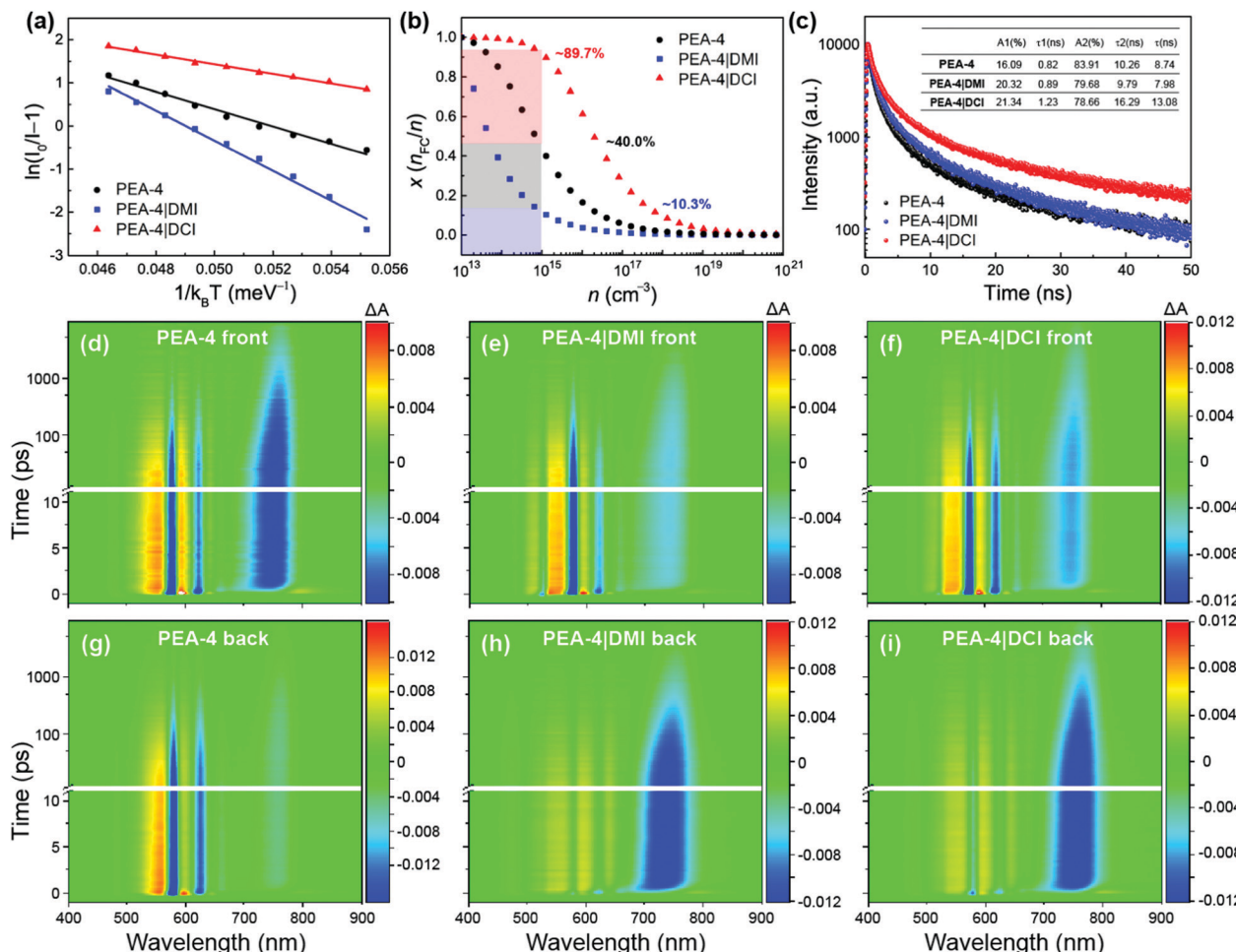


Fig. 4 Carrier dynamics analysis by steady-state and transient measurements. (a) Binding energy (E_B) and (b) the corresponding simulation of the free charge fraction over the total excitation density ($x: n_{FC}/n$) at thermal equilibrium according to the Saha Langmuir equation. (c) TRPL decays of 2D RPP samples under photoexcitation at 505 nm with the inset summarizing the biexponential fitting results. TA spectra of neat and DMI/DCI-treated PEA-4 perovskites from front side (d–f) and back side (g–i), respectively.

exhibits the longest average lifetime τ , indicative of the least grain defects and lattice mismatch.

$$Y = A_1 \exp\left(-\frac{t}{\tau_1}\right) + A_2 \exp\left(-\frac{t}{\tau_2}\right) + C \quad (2)$$

Furthermore, transient absorption (TA) spectroscopy characterization was conducted to gain a finer understanding of the local charge carrier dynamics as shown in Fig. 4d–i and the corresponding SVD fitting results are summarized in Fig. S12 (ESI†). Since we assume that the phase organization would be significantly regulated by the additive treatment, we specifically compared the TA signals with the incident excitation beam hitting the front side (the film) and the back side (the substrate) of the sample. Although the optical density (OD) of thin film is measured to be 0.5, which allows for a complete penetration of the incident light, the major TA response should still be mainly contributed by the area within 50 nm in depth from the surface. The 2D TA spectrograms of all the samples are displayed with front face (Fig. 4d–f) and back face (Fig. 4g–i) photo-excitation. In principle, all the TA spectra exhibit several

narrow ground-state bleach (GB) bands corresponding to various n phases of 2D perovskites (*i.e.*, 460 nm, $n = 1$; 520 nm, $n = 2$; 580 nm, $n = 3$; and 620 nm, $n = 4$) as well as 3D phase at 760 nm. The positive bands refer to the excited-state absorption of each phase. Such a phenomenon confirms the integration on mixed 2D/3D phases among both neat and additive-treated samples. In particular, we observe that in pristine samples, the ratio of 3D phases at the top surface is larger than that at the bottom surface close to the substrate (Fig. 4d *vs.* Fig. 4g). By contrast, such a trend is reversed in additive-treated samples (Fig. 4e and f *vs.* Fig. 4h and i). We also carried out singular value decomposition (SVD) fitting of the TA spectra to extract lifetime components (see ESI† for details). In general, both the front-side and back-side photo-excited samples exhibit ultrafast sub-ps components (black curves in the SVD fitting panels in Fig. S12, ESI†), representing efficient charge transfer from 2D phases to the 3D phase after excitation. However, all the front-side excited samples (red lines in Fig. S12a–c, ESI†) and one back-side pristine sample (red line in Fig. S12d, ESI†) show an extra charge transfer component which should be attributed to the dissociation

of the interfacial charge transfer state. This implicates that the inter-phase charge transfer in that scenario would undergo a two-step process toward complete charge separation. On the other hand, such a process is absent in back-side excited additive-treated samples, suggesting that the charge transfer at the bottom area becomes more efficient after additive treatment. This indicates that the structure regulation by the additive may be more pronounced at the bottom side of the thin film.

Finally, we fabricated the p-i-n architecture planar solar cells with a configuration of ITO (~ 130 nm)/PEDOT:PSS (80–100 nm)/(PEA)₂MA₃Pb₄I₁₃ ($n = 4$, ~ 328 nm)/PCBM (80–100 nm)/BCP (30–50 nm)/Ag (~ 100 nm). Fig. 5a shows the representative current density–voltage (J - V) characteristics of pristine PEA₂MA₃Pb₄I₁₃ ($n = 4$) along with DMI and DCI treatments and the ensuing V_{OC} , J_{SC} and FF under reverse and forward scan directions are summarized in Table 1. As a result, a champion cell is achieved in the DCI-treated PEA-4 with an outstanding PCE of $\sim 17.0\%$ under reverse scanning with a synergistic improvement of J_{SC} (21.93 mA cm⁻²), V_{OC} (1.12 V) and FF (69.0%), which stand among the best of all RP- and DJ-type 2D halide perovskite solar cells, in particular with $n = 4$, as shown in Table S2 (ESI†). The superior cell performance originates primarily from the remarkable enhancements of both J_{SC} and V_{OC} compared to those of neat PEA-4 and PEA-4|DMI based devices. An addition of DCI to PEA-4 is found to prominently increase J_{SC} from ~ 16.7 to ~ 21.9 mA cm⁻² in the device, which is mainly attributed to the phase buffering during the crystallization process, effectively regulating the lattice

orientation with fewer interphase defects and thus strengthening the carrier transportation. In contrast, the competitive effect between inferior exciton splitting and oriented phase lattice in the PEA-4|DMI-based device gives rise to J_{SC} analogous to that of pristine PEA-4. According to the Tauc plot in Fig. S13 (ESI†), the energy gaps for neat and DMI/DCI treated PEA-4 are estimated to be 1.81, 1.83 and 1.77 eV, respectively. The difference between energy gap and V_{OC} yields the voltage loss, which accordingly follows a trend of PEA-4 > PEA-4|DMI > PEA-4|DCI. In addition, the corresponding external quantum efficiency (EQE) profiles are shown in Fig. 5b, which display the photon harvesting in the optical wavelength range of 300–800 nm. The integrated photocurrent values show a minimal mismatch of $\sim 10\%$ with the obtained J_{SC} values from the J - V curves. In comparison to the control PEA-4 device, the PEA-4|DMI based device shows a decline of the EQE values in ranges of 300–350 nm and 400–670 nm (refer to low- n phases) yet an increase from 670–800 nm (refer to 3D-like phases), both of which coincide with the absorbance spectra shown in Fig. 1d. After DCI treatment, in contrast, the EQE is significantly enhanced through the entire absorption range, in which the highest intensity is located at ~ 520 nm corresponding to the optical absorbance of low- n phases. Importantly, negligible current hysteresis is found (Fig. S14, ESI†) and a stabilized power output (SPO) $\sim 16\%$ is attained under a maximum power point of 0.84 V as shown in Fig. 5c. On the other hand, the V_{OC} values in the device follow a descending trend of PEA-4|DCI > PEA-4|DMI > PEA-4, indicating that the voltage loss primarily caused by trap-assisted nonradiative recombination is in order of

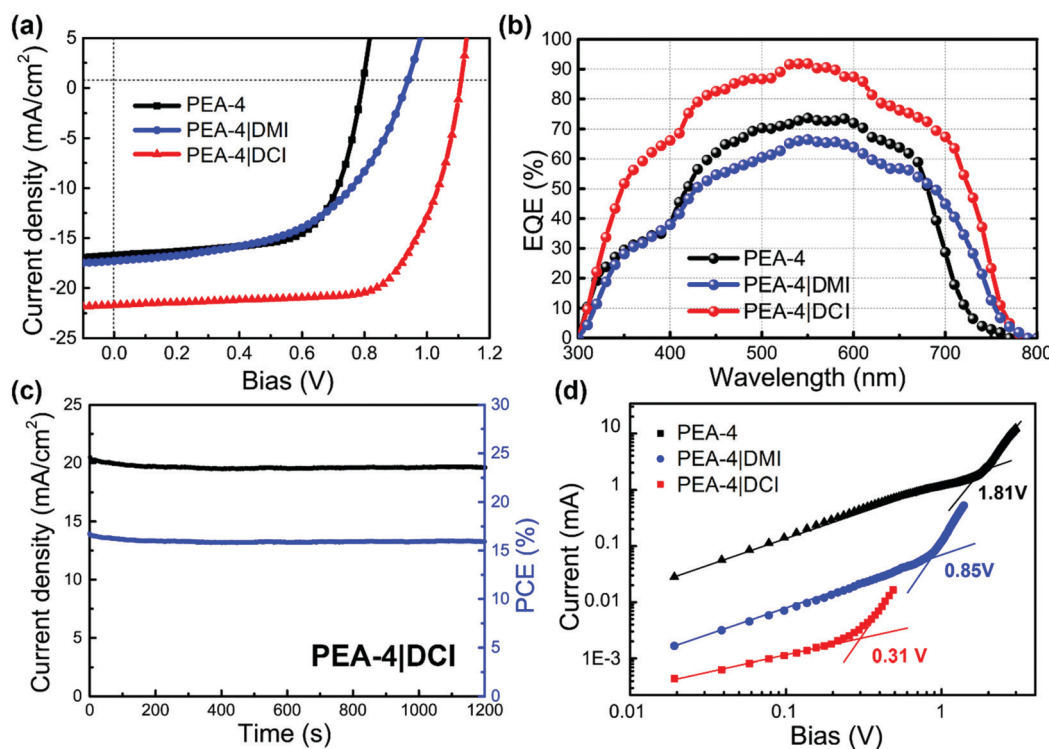


Fig. 5 Solar cell performance. (a) J - V curves, (b) EQE profiles, (c) the photo-current density over 1200 s under a bias of 0.84 V of DCI-treated PEA-4 and (d) dark J - V characteristics of electron-only devices.

Table 1 Summary of photovoltaic parameters of 2D PEA-4 RPP based planar solar cells

Sample	Scanning direction	J_{SC} (mA cm ⁻²)	V_{OC} (V)	FF	PCE (%)
PEA-4	Reverse	16.72	0.80	0.65	8.75
	Forward	16.87	0.80	0.61	8.25
PEA-4 DMI	Reverse	17.28	0.90	0.52	8.48
	Forward	16.85	0.94	0.49	7.83
PEA-4 DCI	Reverse	21.93	1.12	0.69	16.94
	Forward	21.20	1.12	0.68	16.14

PEA-4|DCI < PEA-4|DMI < PEA-4. The PCE of PEA-4|DCI kept over 96% of initial values similar to PEA-4 (~93.8%) whereas the PCE of PEA-4|DMI degraded to ~64.0% over 30 days in a N₂ filled glovebox, as shown in Fig. S15 (ESI†). The space charge limited current (SCLC) analysis is thus evaluated to derive trap-state densities on electron-only devices, due to the ambipolar transport nature of 2D halide perovskites,³⁵ with a device structure of ITO/SnO₂/2D RPP/PCBM/BCP/Ag, as shown in Fig. 5d. The trap-state density can be determined using the equation $N_T = (2\varepsilon_0\epsilon_r V_{TFL})/(qL^2)$, where ε_0 is the vacuum permittivity (*i.e.*, 8.85×10^{-12} F m⁻¹), ϵ_r is the relative dielectric constant (*i.e.*, 25), L is the thickness of the 2D RPP film (~325 nm), V_{TFL} is the onset voltage of the trap-filled limit region (as labeled in Fig. 5d), and q is an elementary charge (*i.e.*, 1.6×10^{-19} C).³⁶ The trap-state densities are calculated to be 4.74×10^{16} , 2.23×10^{16} , and 8.12×10^{15} cm⁻³ for neat PEA-4 and DMI- and DCI-treated PEA-4, respectively, which coincide well with the trend of the V_{OC} loss. The lowest trap density of PEA-4|DCI is believed to arise from the formation of a Lewis acid-base pair between the DCI additive and the inorganic perovskite cage [PbI₆]⁴⁻, and the phase buffering during crystallization, both of which collectively passivate interphase defects and suppress trap-assisted nonradiative recombination, thereby well-interpreting the V_{OC} loss as discussed above.

On a last note, how to determine the reaction mode whether as an additive or a spacer cation remains a peculiar topic for all additive engineering studies in 2D halide perovskites. In an attempt to resolve this concern, we performed the Gaussian calculation of the intermolecular E_{BS} between PbI₂ and cations, and the results are shown in Fig. S16 (ESI†). The formation of the perovskite structure essentially depends on the strength of the interaction (E_B) between cation and PbI₂. For example, MA combines with PbI₂ to construct 3D perovskites (MAPbI₃), while if an additional PEA spacer is introduced, which could compete with MA to interact with PbI₂ owing to the approximate E_B values (~23.74 kcal mol⁻¹ for MA and ~22.89 kcal mol⁻¹ for PEA), 2D perovskite structures would be formed. It is obvious that the E_B of DCI bound to PbI₂ is much smaller (~12.39 kcal mol⁻¹) than that of the cations that construct 2D perovskites (*i.e.*, MA and PEA). In addition, the molar ratio of the introduced DCI in the precursor solution is infinitesimal. Thus, we believe that DCI acts as an additive rather than as a spacer in this 2D perovskite.

Conclusions

This study has demonstrated a phase buffering process *via* introducing a cyano-based DCI additive that allows the

reconciliation of the internal lattice strain and regulates lattice orientation in 2D halide perovskites. A combination of electrostatic potential distribution mapping and DFT analysis reveals that the -CN⁻ unit in DCI acts as a Lewis base and strongly coordinates with the Pb²⁺ Lewis acid by comparing the impacts of methyl-based DMI and cyano-based additives. Given the phase integral area evolution of time-resolved *in situ* GIWAXS, we then propose a model to interpret the phase buffering uncovered in HR-TEM images, that is, the inorganic octahedra and A-site cations are both exchanged with pre-crystallized spacers during the crystallization growth process to reconstruct strain-relieved phases. This buffering model is indirectly verified using the SCLC analysis that trap density caused by the interphase strain is suppressed by an order of magnitude. With the aid of phase buffering, the optimal 2D PEA₂MA₂Pb₃I₁₀ ($n = 4$) based solar cells achieve a remarkable efficiency of ~17%, which represents a ~50% improvement over that of neat PEA-4. Furthermore, the unencapsulated device showed superior stability, retaining 97% of its original PCE under a N₂ atmosphere in a glovebox over 30 days. We believe that this work provides a facile yet effective method to regulate the microscopic film morphology for efficient and stable 2D perovskite photovoltaics. Based on the Lewis acid-base theory, other additive molecules bearing -S-, -SH, -O-, -OH, and R₃P units also offer great potential for the optimization of 2D perovskite crystal growth, in which both the -SCN unit and S atom have been successfully exploited in 2D halide perovskites as summarized in Table S3 (ESI†).

Author contributions

S. Yu synthesized perovskite thin films, characterized the optical properties, obtained SEM images, XRD/GIWAXS profiles and binding energies, and fabricated solar cells along with device measurement and SCLC analysis. J. Meng performed HR-TEM imaging. Y. Yang conducted *in situ* GIWAXS characterization. Q. Pan carried out TA analysis and Q. Zhao recorded the XPS spectra. S. Yu and Z. Liang wrote the manuscript while K. Zheng, Y. Yang and T. Pullerits helped in revising the manuscript. Z. Liang led the entire project. All authors read the manuscript and contributed to the discussion of the results.

Conflicts of interest

There are no conflicts to declare.

Acknowledgements

This work was supported by the Science and Technology Commission of Shanghai Municipality (STCSM) under grant No. 20XD1400500 and 21520710900 and the National Natural Science Foundation of China (NSFC)-The Swedish Foundation for International Cooperation in Research and Higher Education (STINT) under grant No. 5191101797 (Z. L.). K. Z. acknowledges the support from the Danish Council for Independent Research

No. 7026-0037B and Swedish Research Council No. 2017-05337. The work performed in Lund was supported by Swedish Energy Agency Grant No. 446511-1, Swedish research council, STINT, Crafood, and KAW foundation. Y. Y. acknowledges the National Natural Science Foundation of China (grant No. 12175298) and Shanghai Municipal Commission for Science and Technology (grant No. 20ZR1464100). The authors gratefully express their thanks for the beam time and technical support provided by the BL17B1 and BL14B1 GIWAXS beamline at Shanghai Synchrotron Radiation facility (SSRF). They would like to thank Xiyue Ma at Shijianjia Lab (www.shijianjia.com) for the XRD measurements.

References

- Y. Yang, C. Liu, O. A. Syzgantseva, M. A. Syzgantseva, S. Ma, Y. Ding, M. L. Cai, X. P. Liu, S. Y. Dai and M. K. Nazeeruddin, *Adv. Energy Mater.*, 2021, **11**, 2002966.
- Z. Wang, Q. Wei, X. Liu, L. Liu, X. Tang, J. Guo, S. Ren, G. Xing, D. Zhao and Y. Zheng, *Adv. Funct. Mater.*, 2021, **31**, 2008404.
- H. Wu, X. Lian, J. Li, Y. Zhang, G. Zhou, X. Wen, Z. Xie, H. Zhu, G. Wu and H. Chen, *J. Mater. Chem. A*, 2021, **9**, 12566–12573.
- Best Research Cell Efficiencies: <https://www.nrel.gov/pv/assets/pdfs/best-research-cell-efficiencies.20220126.pdf>.
- S. Panuganti, L. V. Besteiro, E. S. Vasileiadou, J. M. Hoffman, A. O. Govorov, S. K. Gray, M. G. Kanatzidis and R. D. Schaller, *J. Am. Chem. Soc.*, 2021, **143**, 4244–4252.
- M. Akiyoshi, M. Yoshizawa-Fujita, Y. Takeoka and M. Rikukawa, *Chem. Commun.*, 2021, **57**, 3395–3398.
- T. Niu, Y. Xie, Q. Xue, S. Xun, Q. Yao, F. Zhen, W. Yan, H. Li, J. L. Bredas, H. L. Yip and Y. Cao, *Adv. Energy Mater.*, 2022, **12**, 2102973.
- W. Fu, H. Liu, X. Shi, D. Zuo, X. Li and A. K. Y. Jen, *Adv. Funct. Mater.*, 2019, **29**, 1900221.
- J. M. Hoffman, C. D. Malliakas, S. Sidhik, I. Hadar, R. McClain, A. D. Mohite and M. G. Kanatzidis, *Chem. Sci.*, 2020, **11**, 12139–12148.
- L. Gao, X. Li, B. Traore, Y. Zhang, J. Fang, Y. Han, J. Even, C. Katan, K. Zhao, S. Liu and M. G. Kanatzidis, *J. Am. Chem. Soc.*, 2021, **143**, 12063–12073.
- G. Lv, L. Li, D. Lu, Z. Xu, Y. Dong, Q. Li, Z. Chang, W. Yin and Y. Liu, *Nano Lett.*, 2021, **21**, 5788–5797.
- Y. Li, J. V. Milic, A. Ummadisingu, J. Y. Seo, J. H. Im, H. S. Kim, Y. Liu, M. I. Dar, S. M. Zakeeruddin, P. Wang, A. Hagfeldt and M. Gratzel, *Nano Lett.*, 2019, **19**, 150–157.
- D. Lu, G. Lv, Z. Xu, Y. Dong, X. Ji and Y. Liu, *J. Am. Chem. Soc.*, 2020, **142**, 11114–11122.
- L. Mao, P. Guo, M. Kepenekian, I. Spanopoulos, Y. He, C. Katan, J. Even, R. D. Schaller, R. Seshadri, C. C. Stoumpos and M. G. Kanatzidis, *J. Am. Chem. Soc.*, 2020, **142**, 8342–8351.
- H. Ren, S. Yu, L. Chao, Y. Xia, Y. Sun, S. Zuo, F. Li, T. Niu, Y. Yang, H. Ju, B. Li, H. Du, X. Gao, J. Zhang, J. Wang, L. Zhang, Y. Chen and W. Huang, *Nat. Photonics*, 2020, **14**, 154–163.
- Y. Chen, Y. Sun, J. Peng, J. Tang, K. Zheng and Z. Liang, *Adv. Mater.*, 2018, **30**, 1703487.
- Z. Li, B. Ma, Y. Xu, Y. Lei, W. Lan, G. Wang, W. Li, Q. Wang, H. Zhang and Z. Jin, *Adv. Funct. Mater.*, 2021, **31**, 2106380.
- C. Liang, H. Gu, Y. Xia, Z. Wang, X. Liu, J. Xia, S. Zuo, Y. Hu, X. Gao, W. Hui, L. Chao, T. Niu, M. Fang, H. Lu, H. Dong, H. Yu, S. Chen, X. Q. Ran, L. Song, B. Li, J. Zhang, Y. Peng, G. Shao, J. Wang, Y. Chen, G. Xing and W. Huang, *Nat. Energy*, 2021, **6**, 38–45.
- L. Mao, R. Kennard, B. Traore, W. Ke, C. Katan, J. Even, M. L. Chabiny, C. C. Stoumpos and M. G. Kanatzidis, *Chem.*, 2019, **5**, 2593–2604.
- M. Kepenekian, B. Traore, J. C. Blancon, L. Pedesseau, H. Tsai, W. Y. Nie, C. C. Stoumpos, M. G. Kanatzidis, J. Even, A. D. Mohite, S. Tretiak and C. Katan, *Nano Lett.*, 2018, **18**, 5603–5609.
- Y. Xu, M. Wang, Y. Lei, Z. Ci and Z. Jin, *Adv. Energy Mater.*, 2020, **10**, 2002558.
- H. Tsai, W. Nie, J. C. Blancon, C. C. S. Toumpos, R. Asadpour, B. Harutyunyan, A. J. Neukirch, R. Verduzco, J. J. Crochet, S. Tretiak, L. Pedesseau, J. Even, M. A. Alam, G. Gupta, J. Lou, P. M. Ajayan, M. J. Bedzyk, M. G. Kanatzidis and A. D. Mohite, *Nature*, 2016, **536**, 312–316.
- A. T. Barrows, S. Lilliu, A. J. Pearson, D. Babonneau, A. D. F. Dunbar and D. G. Lidzey, *Adv. Funct. Mater.*, 2016, **26**, 4934–4942.
- S. Yu, Y. Yan, Y. Chen, P. Chabera, K. Zheng and Z. Liang, *J. Mater. Chem. A*, 2019, **7**, 2015–2021.
- Z. Ning, O. Voznyy, J. Pan, S. Hoogland, V. Adinolfi, J. Xu, M. Li, A. R. Kirmani, J. P. Sun, J. Minor, K. W. Kemp, H. Dong, L. Rollny, A. Labelle, G. Carey, B. Sutherland, I. Hill, A. Amassian, H. Liu, J. Tang, O. M. Bakr and E. H. Sargent, *Nat. Mater.*, 2014, **13**, 822–828.
- R. A. Kerner, T. Schloemer, P. Schulz, J. Berry, J. Schwartz, A. Sellinger and B. P. Rand, *J. Mater. Chem. C*, 2019, **7**, 5244–5250.
- H. Chena, Y. Xia, B. Wu, F. Liu, T. Niu, L. Chao, G. Xing, T. Sum, Y. Chen and W. Huang, *Nano Energy*, 2019, **56**, 373–381.
- J. Wang, S. Luo, Y. Lin, Y. Chen, Y. Deng, Z. Li, K. Meng, G. Chen, T. Huang, S. Xiao, H. Huang, C. Zhou, L. Ding, J. He, J. Huang and Y. Yuan, *Nat. Commun.*, 2020, **11**, 582.
- H. Lai, B. Kan, T. Liu, N. Zheng, Z. Xie, T. Zhou, X. Wan, X. Zhang, Y. Liu and Y. Chen, *J. Am. Chem. Soc.*, 2018, **140**, 11639–11646.
- Y. Miao, Y. Chen, H. Chen, X. Wang and Y. Zhao, *Chem. Sci.*, 2021, **12**, 7231–7247.
- M. Qin, P. Chan and X. Lu, *Adv. Mater.*, 2021, **33**, 2105290.
- X. Zhang, R. Munir, Z. Xu, Y. Liu, H. Tsai, W. Nie, J. Li, T. Niu, D. M. Smilgies, M. G. Kanatzidis, A. D. Mohite, K. Zhao, A. Amassian and S. F. Liu, *Adv. Mater.*, 2018, **30**, 1707166.
- C. Liu, Y. Yang, K. Rakstys, A. Mahata, M. Frankevicius, E. Mosconi, R. Skackauskaite, B. Ding, K. G. Brooks, O. J. Usiobo, J. N. Audinot, H. Kanda, S. Driukas, G. Kavaliauskaitė, V. Gulbinas, M. Dessimož, V. Getautis, F. De Angelis, Y. Ding, S. Dai, P. J. Dyson and M. K. Nazeeruddin, *Nat. Commun.*, 2021, **12**, 6394.
- V. D'Innocenzo, G. Grancini, M. J. P. Alcocer, A. R. S. Kandada, S. D. Stranks, M. M. Lee, G. Lanzani, H. J. Snaith and A. Petrozza, *Nat. Commun.*, 2014, **5**, 3586.
- J. M. Frost and A. Walsh, *Acc. Chem. Res.*, 2016, **49**, 528–535.
- R. H. Bube, *J. Appl. Phys.*, 1962, **33**, 1733–1737.